SCIENCE CHINA
Physics, Mechanics & Astronomy

•Article•

February 2022 Vol. 65 No. 2: 224611
https://doi.org/10.1007/s11433-021-1785-y

Non-Hermitian topological coupler for elastic waves

Yan Meng[1,2], Xiaoxiao Wu[3], Yaxi Shen[2], Dong Liu[2], Zixian Liang[1], Xiang Zhang[3*], and Jensen Li[2*]

[1] *Institute of Microscale Optoelectronics, Shenzhen University, Shenzhen 518060, China;*
[2] *Department of Physics, The Hong Kong University of Science and Technology, Clear Water Bay, Hong Kong 999077, China;*
[3] *Faculties of Sciences and Engineering, The University of Hong Kong, Hong Kong 999077, China*

Received July 4, 2021; accepted September 9, 2021; published online December 13, 2021

Non-Hermitian topological systems, by combining the advantages of topological robustness and sensitivity induced by non-Hermiticity, have recently emerged and attracted much research interest. Here, we propose a device based on the topological coupler in elastic waves with non-Hermiticity, which contains two topological domain walls and four ports. In this device, topological robustness routes the transmission of waves, while non-Hermiticity controls the gain or loss of waves as they propagate. These mechanisms result in continuous and quantitative control of the energy distribution ratio of each port. A non-Hermitian Hamiltonian is introduced to reveal the coupling mechanism of the topological coupler, and a scattering matrix is proposed to predict the energy distribution ratio of each port. The proposed topological coupler, which provides a new paradigm for the non-Hermitian topological systems, can be employed as a sensitive beam splitter or a coupler switch. Moreover, the topological coupler has potential applications in information processing and logic operation in elastic circuits or networks, and the paradigm also applies to other classical systems.

topological edge states, non-Hermitian systems, topological coupler

PACS number(s): 03.65.Vf, 68.35.Rh, 62.30.+d, 42.82.Et

Citation: Y. Meng, X. Wu, Y. Shen, D. Liu, Z. Liang, X. Zhang, and J. Li, Non-Hermitian topological coupler for elastic waves, Sci. China-Phys. Mech. Astron. **65**, 224611 (2022), https://doi.org/10.1007/s11433-021-1785-y

1 Introduction

The concept of topological physics stems from quantum condensed matters [1-4], revealing that the topological insulators can support topologically protected edge states and interface states. These states are unidirectional, backscattering-immune [5], and robust against the local defects, disorders, and perturbations of the boundaries [6]. As classical analogies of the quantum topological insulators [7], the associated unidirectional propagating edge states have been extended into different classical wave regimes such as photonics [8,9], airborne acoustics [10-14], water waves [15] and elastic waves [16-21]. Up to date, topology has found applications in waveguide coupling [22], robust Fano resonance [23], vortex lasing [24], and one-way propagation of signals for communications and spin-wave manipulation devices [25,26]. Therefore, topologically protected edge states with backscattering-immune and spin-momentum locking effects provide robustness of operating classical waves.

On the other hand, non-Hermiticity is another concept extended from quantum condensed matters to classical wave regimes, which refers to the gain and loss contrast of an active system or the loss contrast in a totally passive system [27]. Non-Hermiticity focuses on the system sensitivity in

*Corresponding authors (Jensen Li, email: jensenli@ust.hk; Xiang Zhang, email: president@hku.hk)

terms of the material gain or loss, and it can manipulate wave propagation as proposed in the optical [28-30], acoustic [31,32], and elastic systems [33]. With increasing non-Hermiticity, the system will evolve from the so-called PT-symmetric phase into PT-broken phase by going through an exceptional point, where multiple eigenstates (and eigenvalues) coalesce [34]. The existence of exceptional points is accompanied by many intriguing phenomena, such as unidirectional invisibility [31,35], unidirectional energy transfer [36], single-mode lasing [37], and loss-induced lasing [38]. In elastic waves, the loss and gain contrast can be realized by piezoelectric elements that are composed of piezoelectric sensors and actuators with active feedback control loops [39,40]. Comparatively, the loss contrast in a totally passive system can be implemented by loading porous rubber sheets on the surface of metamaterials [41].

Very recently, by combining the above two concepts of topology and non-Hermiticity with metamaterials and photonic/phononic crystals, many special types of topological boundary and corner states have been proposed with optical [42], acoustic [43,44], mechanical [45], and elastic systems [46]. From a fundamental perspective, topological systems with non-Hermiticity can be used to generate new kinds of topological entities such as bulk Fermi arcs [47], bulk-edge correspondence in the non-Hermitian version [48], and non-Hermitian skin effect [49]. Furthermore, the introduction of non-Hermiticity to topological systems offers a new degree of freedom to control wave propagation, such as concurrent existence of exceptional point and topological edge states, novel non-Hermiticity-induced topological entities [50,51].

In this article, we develop a non-Hermitian topological coupler in elastic waves, which contains a sandwich configuration of a topological insulator (TI) in between two regions of ordinary insulators (OI). We also investigate how the introduction of non-Hermiticity (balanced gain and loss) can be used to quantitatively control the coupling of topological interface states. As we shall see, topology provides robust interface states with backscattering-immune and spin-momentum locking properties, while non-Hermiticity provides sensitivity to control energy distribution ratios with gain or loss. In addition, a non-Hermitian Hamiltonian model and a scattering matrix are established to reveal the energy distribution ratios of the topological coupler. The proposed topological coupler with quantitative tunability of elastic waves is a promising candidate for information processing and logic operation, which may find potential applications in integrated topological circuits or networks.

2 Theory and model

We start from a hexagonal-lattice phononic crystal, as illustrated in Figure 1(a), a red dashed hexagonal box marks one unit cell, which is composed of six identical equilateral triangles connected by twelve cuboid beams. The geometry parameters are correspondingly labeled in Figure 1(a), and the dimensions are chosen as: a=12 mm, $A=\sqrt{3}\,a$, h=2 mm, b=6 mm, g=1.6 mm, and $d_c=A/3$. The key geometry parameter is r, which indicates the distance from the center of the unit cell (green dot) to the center of the equilateral triangle (red dot). The material is a kind of cured photosensitive resin with material parameters of density ρ_0=1190 kg/m^3, Young's modulus E_0=3.4 GPa, and Poisson's ratio v=0.35 [52]. We assume $e^{-i\omega t}$ time-harmonic convention. The simulated (with commercial software COMSOL Multiphysics) band structure of the phononic crystal with $r=d_c$ is shown in Figure 1(b), doubly degenerate Dirac cones (indicated by a blue dot) can be achieved at the Γ point [53]. The Dirac cones can be gapped when r deviates from d_c, as the band structure shown in Figure 1(c) for $r=0.8d_c$ and band structure shown in Figure 1(d) for $r=1.2d_c$. The out-of-plane displacement (real(w)) for eigenstates of p_x, p_y, $d_{x^2+y^2}$, d_{xy} at the Γ point are shown in the insets of Figure 1(c) and (d), respectively. The inverse order of p/d modes in Figure 1(d) implies the topological phase translates from trivial ($r=0.8d_c$) to nontrivial ($r=1.2d_c$) [53].

Figure 1(e) shows the domain wall constructed by an OI and a TI region, where the interface is marked by a red curve. A super unit cell with a height of $\Lambda=3a$ is marked by a black hollow box. The projected band structure for this super unit cell is shown in Figure 1(f), interface states (blue stars) can be seen within the bulk bands (gray dots). The interface states with positive group velocity are pseudospin up and those with negative group velocity are pseudospin down. A pseudospin up (down) state is indicated by a red (green) star and marked with an anti-clockwise (a clockwise) arrow to denote its phase evolution, which reveals the spin-momentum locking property of the topological interface states. The bands for interface states near the Γ point are approximately linear. Their fitting lines with a function of $f=\pm v_F k_y+\omega_F/2\pi$ are plotted by red lines in Figure 1(f). The fitting coefficients are v_F=22.6 m/s and $\omega_F=2\pi\times8.8$ kHz, which will be used to build the analytical model later. The spin-momentum locking feature can also be proved by the configuration shown in Figure 1(g), where a source with clockwise (pseudospin down) or anti-clockwise (pseudospin up) phase winding [53,54] is placed in the middle of the domain wall. The interface states with positive and negative group velocity are selectively excited and shown in the left and right panels of Figure 1(g), respectively. These topological interface states will be used as a foundation for designing the topological coupler.

We then combine two domain walls together to construct a super unit cell as shown in Figure 2(a). The field maps (real (w)) for four eigenstates of the super unit cell with N=5, at

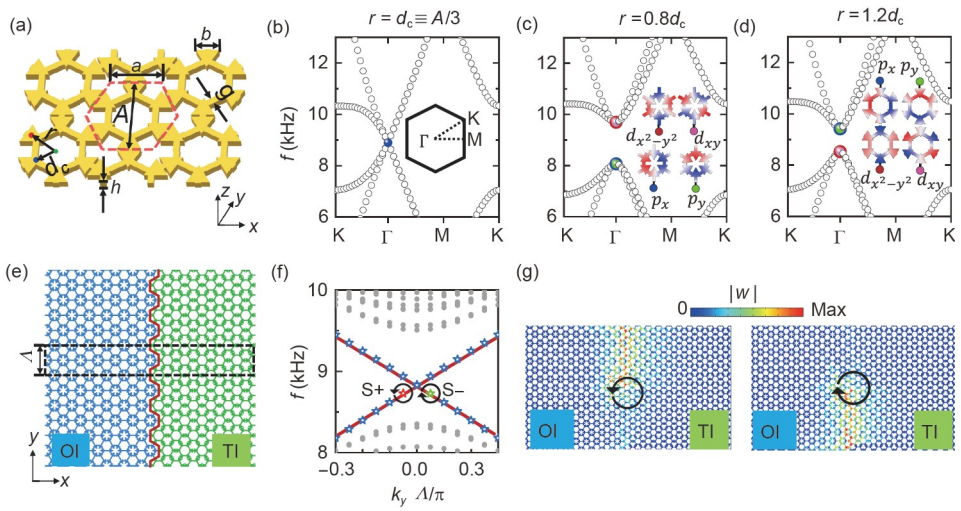

Figure 1 (Color online) (a) Schematic illustration of the phononic crystal plate. The unit cell (marked by a red dashed hexagonal box) with a side length a=12 mm, lattice constant $A = \sqrt{3}\,a$, and thickness h=2 mm, which is composed of six equilateral triangles and twelve cuboid beams. The equilateral triangles with a side length b=6 mm and the cuboid beams with a width g=1.6 mm. The distance from the unit cell center (green dot) to the equilateral triangle (red dot) center is r, and to the junction of two beams (blue dot) is d_c=A/3. (b)-(d) Band structure for r=d_c (b), r=0.8d_c (c), and r=1.2d_c (d). The insets show the p and d eigenmodes at the Γ point. (e) A topological domain wall (indicated by a red curve) constructed by an OI (left) and a TI (right) region. A super unit cell with a height of Λ=3a is marked by a black dashed box. (f) Projected band structure of the super unit cell in (e). Gray dots: bulk bands; blue stars: interface states. The pseudospins of the interface states at 8.7 kHz, with k_y=±0.05π/Λ (red and green stars) are indicated by anti-clockwise (pseudospin up) and clockwise (pseudospin down) arrows, respectively. (g) The out-of-plane displacement ($|w|$) of the topological interface states at 8.7 kHz excited by a pseudospin up source (left panel) or a pseudospin down source (right panel).

k_y=0.3π/Λ are listed as illustrative examples. It can be seen that elastic waves are concentrated in the vicinity of two interfaces (indicated by black dashed lines) and exponentially decay away from them, implying the simultaneous existence of two interface states. The eigenstates in the first (f=9.5 kHz) and last (f=8.14 kHz) panels are antisymmetric (indicated by "A") along the x-direction, while the eigenstates in the second (f=9.44 kHz) and third (f=8.21 kHz) panels are symmetric (indicated by "S") along the x-direction. Pseudospins of the interface states are indicated by clockwise (pseudospin down) or anti-clockwise (pseudospin up) arrows, and the interface states concentrated at two interfaces possess opposite pseudospins.

The simulated band structures for the super unit cell of the OI-TI-OI configuration with N=10, 5, and 1 are shown in Figure 2(b)-(d), respectively. Topological interface states (blue stars) can be seen within the projected bulk bands (gray dots). We note that each band of the interface states is approximately doubly degenerate as we are putting two topological domain walls together. The increase of bandgap width (around 2η of size in frequency) at the Γ point can be seen as N decrease.

To analytically investigate the bandgap of the interface states supported by the OI-TI-OI configuration, we establish a basis of $\{L_+, L_-, R_+, R_-\}$, where "L" and "R" indicate the interface states on the left and right domain wall, and the subscript "+" and "−" indicate up and down pseudospin properties of the interface states. Equivalently, this basis is the four interface states similar to Figure 2(b) as $N \to \infty$. The Hamiltonian for the topological interface states on the basis of $\{L_+, L_-, R_+, R_-\}$ can be written as [55]:

$$\widehat{H} = \frac{\omega_F}{2\pi} I_4 + \begin{pmatrix} k_y v_F & 0 & \eta & \zeta \\ 0 & -k_y v_F & \zeta & \eta \\ \eta & \zeta & -k_y v_F & 0 \\ \zeta & \eta & 0 & k_y v_F \end{pmatrix}, \tag{1}$$

where ω_F and v_F are the fitting parameters extracted from a single OI-TI domain wall case (Figure 1(f)). I_4 is a four-by-four identity matrix. η corresponds to the coupling strength between the interfaces with the same pseudospin at different domain walls. ζ indicates the coupling strength between the interface states with different pseudospins at different domain walls, which is due to the finite-size effect. With this Hamiltonian, the band structures of the interface states can be given by the governing equation of $\widehat{H}\psi = f\psi$, where ψ=(C_1, C_2, C_3, C_4), C_1, C_2, C_3, and C_4 are the coefficients of the elements in $\{L_+, L_-, R_+, R_-\}$ respectively, f is frequency. The coupling strength η and ζ can be obtained by fitting the simulated eigenfrequency at the Γ point. The band structures reproduced by the eigenvalues of the Hamiltonian $\widehat{H}$ are respectively plotted by red, green, black, and magenta dashed lines in Figure 2(b)-(d). The good agreement between the model results and the simulated results confirms the validity of the Hamiltonian model. The extracted coupling strengths from the Hamiltonian model for N=5 are η=95 Hz

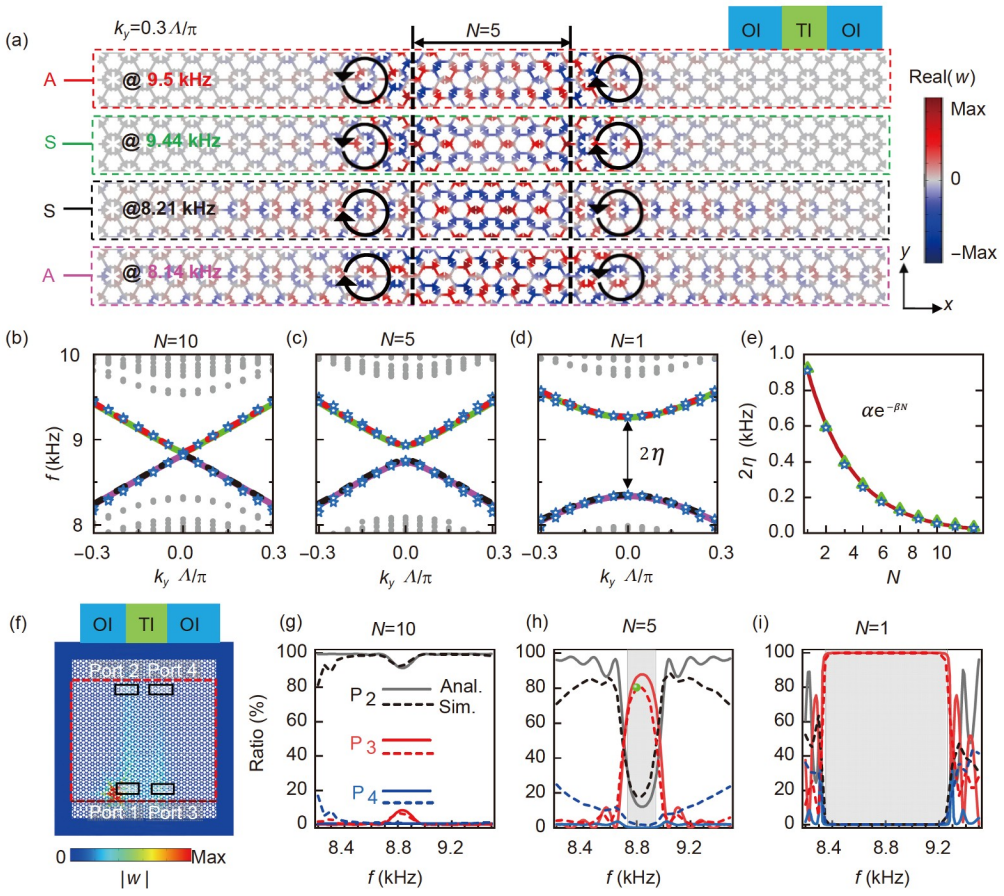

Figure 2 (Color online) (a) Super unit cells of the OI-TI-OI configuration, a TI region with N-unit cells (N=5) in between two OI regions with ten-unit cells. Field maps (real(w)) for four eigenmodes at k_y=0.3π/Λ, f=9.5, 9.44, 8.21, and 8.14 kHz are listed. Symmetric (anti-symmetric) field maps along the x-axis are labeled as "S" ("A"). The clockwise and anti-clockwise arrows indicate the phase evolutions of the interface states concentrate at two interfaces. (b)-(d) The projected band structures for N=10, 5, and 1, respectively. Gray dots: projected bulk bands; blue stars: interface states. The lines are extracted from the Hamiltonian model. (e) Blue stars: the simulated bandgap. Green triangles: coupling strength (η) extracted from the Hamiltonian model. Red line: the exponentially fitting ($2\eta=\alpha e^{-\beta N}$) of the simulated bandgap. (f) Field map of the out-of-plane displacement ($|w|$) for the topological coupler with N=5. Red dashed rectangle: coupling region with 25A in width and 33a_0 in height; black rectangles: four ports. (g)-(i) The energy distribution ratios for the topological coupler with N=10, 5, and 1, respectively. A pseudospin up source is placed near port-1. The short dashed lines are simulated results, and the solid lines are extracted from the scattering matrix. The gray regions indicate the bandgaps of the interface states in (c) and (d).

and ζ=8 Hz. Clearly, η is much larger than ζ, which implies that the bandgap is dominantly caused by the coupling between interface states with the same pseudospin. The simulated bandgap widths (blue stars) and coupling strength (η) extracted from the Hamiltonian model (green triangles) against N are shown in Figure 2(e). An exponential fitting (red line) with $2\eta=\alpha e^{-\beta N}$ shows that the bandgap widths and the coupling strengths decrease exponentially as the unit cell of TI (N) increases, the corresponding fitting results are α=1.35 kHz and β=0.4.

A topological coupler composed of two domain walls with a finite height in y is proposed and shown in Figure 2(f). The coupling region of size 25A (in width) by 33a_0 (in height) is marked by a red dashed box, out of which is absorbing material to reduce the reflection from the outer boundaries. Four terminals of the two domain walls are marked by black rectangles and correspondingly labeled as port-1 to port-4. Here, a pseudospin up source is placed near port-1 to excite the pseudospin up interface states. The field map $|w|$ for N=5 at 8.8 kHz is shown as an illustrative example in Figure 2(f), it can be seen that the interface states are mainly coupled from port-1 into port-3.

To quantitatively describe the coupling energy ($\propto|w|^2$) between each port, we define the energy distribution ratio for each port as:

$$P_i=\frac{\left|w_{P_i}\right|^2}{\sum_j\left|w_{P_j}\right|^2}, \tag{2}$$

where w_{P_i} is the out-of-plane displacement of elastic waves at the i^{th} port, and the summation excludes the port where the source is placed, for example, in Figure 2(f) the source is placed at port-1, then i, j=2, 3, 4. The simulated results for P_2 (black), P_3 (red), and P_4 (blue) are plotted by short dashed

lines in Figure 2(g)-(i) for N equal to 10, 5, and 1, respectively.

On the other hand, the energy distribution ratios can also be extracted from the Hamiltonian model. Specifically, by substituting k_y into $-\mathrm{i}\partial_y$, the governing equation about k_y can be changed into that about y, then a transfer matrix can be established, which describes the propagation of waves within the topological coupler with a finite height in the y-direction. By changing the basis of the transfer matrix, a scattering matrix **S** can be formulated, then the energy distribution of each port can be solved by the scattering matrix. Details of the derivation of the scattering matrix are provided in Appendix. In Figure 2(f), we place a pseudospin up source near port-1 to excite the topological coupler. The coefficients of the incident wave can be expressed as $(1, 0, 0, 0)^{\mathrm{T}}$, and the outgoing waves at the i^{th} port then can be directly calculated by S_{i1}. The energy distribution ratios for port-2 to port-4 can be extracted from the scattering matrix by

$$
\begin{aligned}
P_2 &= \frac{|S_{21}|^2}{|S_{21}|^2+|S_{31}|^2+|S_{41}|^2},\\
P_3 &= \frac{|S_{31}|^2}{|S_{21}|^2+|S_{31}|^2+|S_{41}|^2},\\
P_4 &= \frac{|S_{41}|^2}{|S_{21}|^2+|S_{31}|^2+|S_{41}|^2}.
\end{aligned}
\tag{3}
$$

The model results for P_2 (black), P_3 (red), and P_4 (blue) are plotted by solid lines in Figure 2(g)-(i) for N equal to 10, 5, and 1, respectively. The good agreement between the simulated results and the model results implies the scattering matrix extracted from the Hamiltonian is valid to predict the energy distribution ratios of the topological coupler. It can be seen that as N decreases from 10 to 1, the energy distribution ratios gradually convert from P_2 dominance into P_3 dominance within the bandgaps (indicated by gray boxes), and P_4 is always suppressed, which verifies the topological robustness can control the coupling route to each port. In addition, the energy distribution ratios for the same configuration but excited by a pseudospin down source can be predicted by time-reversal symmetry, for this case, the source should be placed near port-2.

3 Results and discussions

To realize a sensitive and continuous tunability of the energy distribution ratios, we introduce non-Hermiticity into the topological coupler as an additional degree of freedom to control the energy distribution ratios. Specifically, we introduce a balanced loss and gain in the imaginary part of Young's modulus into the OI regions: on the left side with $E_1 = E_0(1+\mathrm{i}\gamma)$ and on the right side with $E_2 = E_0(1-\mathrm{i}\gamma)$. Where $\gamma>0$ ($\gamma<0$) corresponds to gain (loss) on the left side and loss (gain) on the right side. The simulated eigenfrequency (solved from eigenmode solver in COMSOL) against γ at k_y=0 for the configuration with N=5 (same structure with Figure 2(a)) are plotted by black triangles and red dots on the left (real part) and right (imaginary part) panels of Figure 3(a). It can be seen, as the absolute value of γ increase, the eigenfrequencies of the interface states evolve from purely real into complex, the critical points, where multiple eigenfrequencies and eigenmodes coalesce, are termed as exceptional points and indicated by green arrows. As γ is set to be 0.03, 0.057, 0.08, the PT-exact phase, exceptional point, and the PT-broken phase are obtained, respectively. Besides, non-Hermiticity can be introduced into the Hamiltonian in eq. (1) by adding an imaginary part into k_y, i.e., $\mathrm{Im}(k_y) \cong \pm\kappa\gamma$, with a negative (positive) sign for pseudospin up (down), and the fitting result is $\kappa \cong 75\ \mathrm{m}^{-1}$. With all other parameters inheriting from the Hermitian coupler with the same N, the complex band structures can be extracted from the non-Hermitian Hamiltonian. The results are plotted by red and black lines in the same figure, which agrees well with the full-wave simulations.

The simulated eigenfrequency spectra of the interface states against k_y with γ=0.03, 0.057, 0.08 are correspondingly plotted on the left (real part) and right (imaginary part) panels of Figure 3 (b)-(d). It can be seen, at k_y=0, the real part of the interface states has four branches and the imaginary part degenerates at zero for the PT-exact phase. At the exceptional points both the real part and imaginary parts coalesce at k_y=0. For the PT-broken phase, the real part coalesces while the imaginary part splits into four branches, implying either gain or loss of the interface states at two domain walls. The complex eigenfrequencies of the interface states extracted from the non-Hermitian Hamiltonian are plotted as red lines. The good agreement with the simulated results reveals that the Hamiltonian in eq. (1) is also valid near the Γ point by simply introducing an imaginary part into k_y.

The field patterns (real(w)) of the eigenstates for γ=0.03, 0.57, and 0.08 at k_y=0 are shown as color maps in Figure 3(e). The amplitude for the field profiles ($|w|$) at y=0 are plotted by blue lines and shown on the right panels of the field patterns. It can be seen that interface states are concentrated at the two domain walls. For the PT-symmetric phase with γ=0.03 and γ=0.057, field profiles of the four eigenstates are approximately symmetric along x, which implies that the non-Hermiticity induces no concentration of the interface states towards a single domain wall. For the PT-broken phase with γ=0.08, the first and last panels correspond to the eigenstates with positive imaginary eigenfrequency, the interface states concentrated at the left OI-TI domain wall are enhanced and the interface states concentrated at the right TI-OI domain

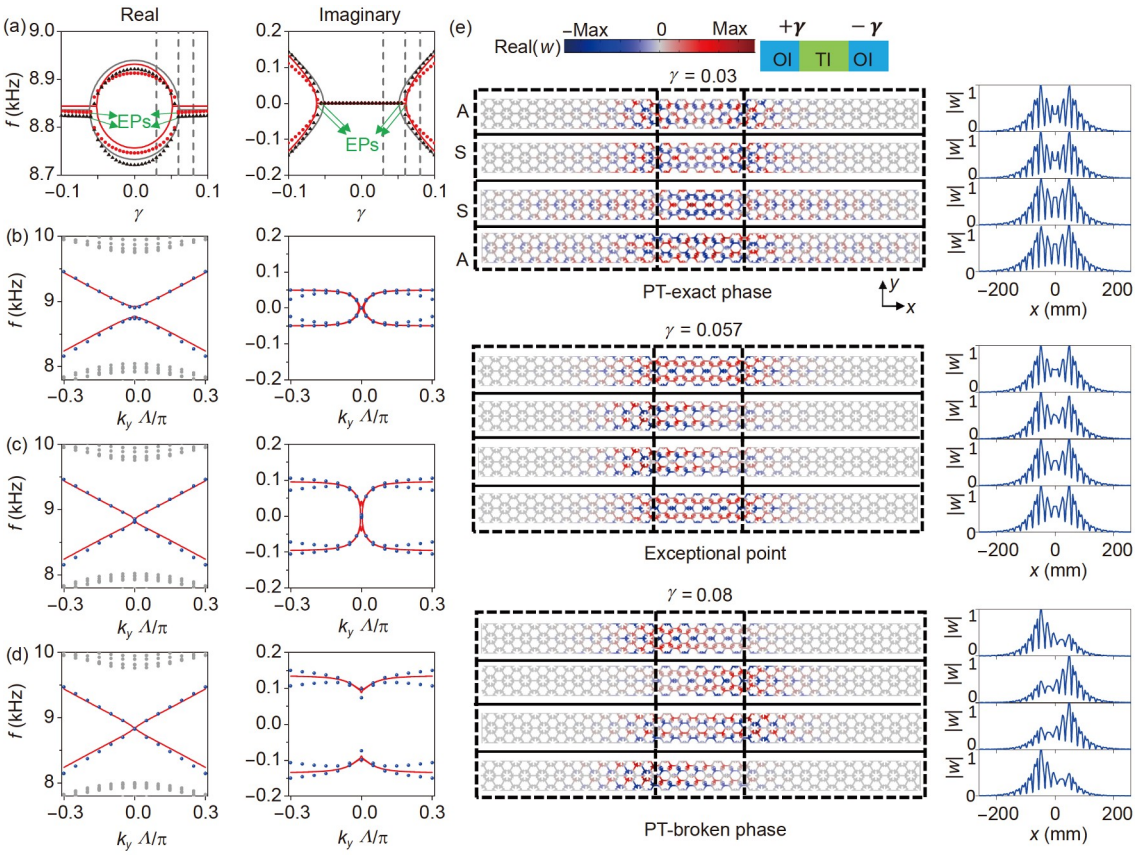

Figure 3 (Color online) (a) Eigenfrequency spectra against γ at k_y=0, for an OI-TI-OI-type configuration with N=5. Left panel: real part; right panel: imaginary part. The black triangles and red dots are simulated results and the lines are extracted from the Hamiltonian model with non-Hermiticity. The simulated exceptional points at γ=±0.057 are indicated by green arrows. The gray dashed lines indicate the PT-exact phase (γ=0.03), the exceptional points (at γ=0.057) and the PT-broken phase (γ=0.08). Band structures for the configuration with N=5, γ=0.03 (b), γ=0.057 (c), and γ=0.08 (d). The symbols indicate the simulated results and the lines are extracted from the Hamiltonian model with non-Hermiticity. (e) Field patterns (real (w)) of the eigenstates with γ=0.03, γ=0.057, and γ=0.08 at k_y=0. The corresponding field profiles ($|w|$) at y=0 are shown as blue lines on the right panels.

wall are suppressed. The second and third panels correspond to the eigenstates with negative imaginary eigenfrequency. The enhancement and suppression of the interface states are at the opposite domain walls. The field maps and the profiles demonstrate the impact of non-Hermiticity on the interface states at the two domain walls, and the concentration of interface states can be used to modulate the energy distribution ratios of a non-Hermitian topological coupler.

By assembling the super unit cells with different N, a topological coupler device can be proposed, whose configuration is schematically illustrated in Figure 4(a). The TI region is indicated by green and the OI regions are indicated by blue, the number of the unit cells for TI spacing in the center of the device is denoted as N_c (here N_c=3), the intersections of the TI and OI regions are along ±60°. Each port is indicated by a black box and labeled as port-1 to port-4, respectively. The pink star indicates the location of the pseudospin up source. For the current topological coupler with a wedge-shaped TI region, the coupling strengths (η and ζ) are modeled as functions varying in y, so when calculating the scattering matrix, the Hamiltonian $\widehat{H}$ in eq. (1) is also modeled as a function varying in y. The final transfer matrix can be obtained by multiplying transfer matrices of each layer with a height of Λ. With the corresponding scattering matrix converted from the final transfer matrix, the energy distribution ratios can be solved. The energy distribution ratios against frequency for port-2, port-3, and port-4 of the topological coupler device with γ=0 are plotted by black, red, and blue lines in Figure 4(b). The short dashed lines are the simulated results and the solid lines are the model results. It can be seen that near the bandgap center (~8.8 kHz) most energy couples from port-2 to port-3, which implies that near the bandgap center the coupling strength reaches its maximum, and we get an energy distribution ratio of P_2=P_3=50%. While P_4 is always suppressed within the frequency regime we are interested in, which is due to the spin-momentum locking property of the interface states. The good agreement between the simulated and model results verifies the validity of the scattering matrix for the topological coupler with a wedge-shaped TI region.

We then introduce non-Hermiticity into the OI regions similar to Figure 3. The energy distribution ratios of P_2 and

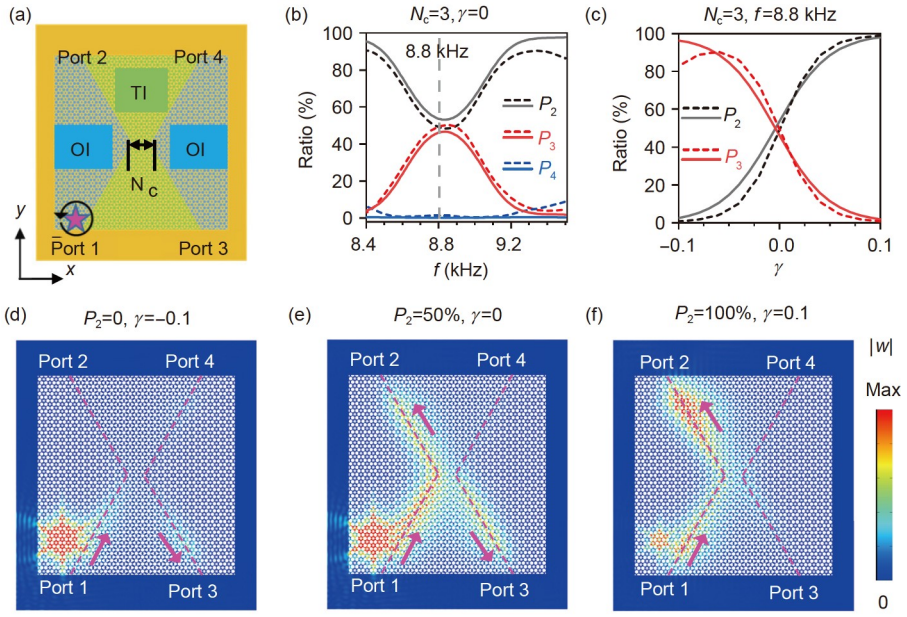

Figure 4 (Color online) (a) Configuration of the proposed topological coupler with an increasing layer of TI (green) from the center (N_c=3) to the boundary (N=16). The intersections of the TI and OI regions are along ±60°. The pink star marks the location of the pseudospin up source, ports are correspondingly denoted from port-1 to port-4. (b), (c) Energy distribution ratios against frequency with γ=0 (b), and against γ at 8.8 kHz (c) for the topological coupler device with N_c=3. The short dashed lines are simulated results and the solid lines are extracted from the scattering matrix. (d)-(f) The field patterns for the topological coupler with N_c=3 at 8.8 kHz. (d) P_2=0% for γ=−0.1. (e) P_2=50% for γ=0. (f) P_2=100% for γ=0.1. The intersections are marked by magenta dashed lines and the main wave propagation directions are indicated by magenta arrows.

P_3 against γ are plotted by black and red lines in Figure 4(c). The spectra show that as γ evolves from −0.1 to 0.1, P_2 can be tuned nearly from 0 to 100%, and P_3 also can be tuned from nearly 0 to 90%. The energy distribution ratios for the topological coupler device with non-Hermiticity verify the achievement of continuous and quantitative tunability by combining the topological robustness and non-Hermiticity. The short dashed lines are the simulated results, and the solid lines are reproduced from the scattering matrix extracted from the Hamiltonian model with non-Hermiticity. The good agreement between the simulated and the model results verifies that the non-Hermitian Hamiltonian model is still valid to analyze the exotic scattering process of the topological coupler and to predict the energy distribution ratios of the non-Hermitian topological coupler. In addition, non-Hermiticity can also be introduced by increasing the loss contrast on two OI regions in a totally passive system [27,41]. The 0 to 100% tunability of P_2 can still hold.

The field maps ($|w|$) for P_2=0% at γ=−0.1, P_2=50% at γ=0, and P_2=100% at γ=0.1 are shown in Figure 4(d)-(f) as examples for the quantitative control of the energy distribution ratios. The domain walls are marked by magenta dashed lines, and the wave propagation directions are indicated by magenta arrows. It can be seen from the field maps, for γ=−0.1, the interface states excited from port-1 mainly transport into port-3, and the waves transporting to port-2 are decreased by non-Hermiticity; for γ=0, the interface states transport equally into port-2 and port-3; for γ=0.1, the interface states mainly transport into port-2, and the waves transporting to port-3 are decreased by non-Hermiticity. These field maps are consistent with the energy distribution spectra shown in Figure 4(c). The energy distribution ratio spectra and the field maps demonstrate the quantitative control of the non-Hermitian topological coupler. The topological coupler with N_c=3 is deliberately designed to satisfy P_2=P_3=50% at γ=0, which requires the smallest non-Hermiticity ($|\gamma|$) to achieve P_2 ranging from 0 to 1. The tuning mechanism is also valid for other values of N_c but it needs a larger $|\gamma|$. In addition, the wedge-shaped TI region also frees the dependence of energy distribution ratios on the height of the coupling region in the straight cases, which makes the control more stable in applications. By coordinating the topological protection and the non-Hermiticity, a topological coupler device with flexible tunability is achieved, which can be used as an on-demand coupler switch or a logical circuit and may find promising applications in encrypted communication and signal processing.

4 Conclusions

In summary, we propose a non-Hermitian topological coupler that is constructed by combining two domain walls. The interface states supported by the two domain walls provide topological transmission of the coupler. By tuning the distance between the two domain walls and inducing non-

Hermiticity, energy distribution ratios of the topological coupler can be quantitatively modulated from 0 to 100%. A non-Hermitian Hamiltonian is introduced to analyze the exotic scattering process of the topological coupler and predict the energy distribution ratios of the coupler. The proposed topological coupler device, which provides a new paradigm for the application of non-Hermitian topological systems, can serve as an element in phononic crystal networks or circuits. To conclude, this paradigm has potential applications in advanced acoustic signal processing, sensing, and even logic operation.

This work was supported by the Research Grants Council of Hong Kong (Grant Nos. 16302218, and C6013-18G), and the Croucher Foundation. Z. Liang acknowledges the financial support by the National Natural Science Foundation of China (Grant Nos. 11574216, and 61505114).

1 K. von Klitzing, Rev. Mod. Phys. **58**, 519 (1986).
2 M. Z. Hasan, and C. L. Kane, Rev. Mod. Phys. **82**, 3045 (2010), arXiv: 1002.3895.
3 X. L. Qi, and S. C. Zhang, Rev. Mod. Phys. **83**, 1057 (2011), arXiv: 1008.2026.
4 S. N. Kempkes, M. R. Slot, J. J. van den Broeke, P. Capiod, W. A. Benalcazar, D. Vanmaekelbergh, D. Bercioux, I. Swart, and C. Morais Smith, Nat. Mater. **18**, 1292 (2019), arXiv: 1905.06053.
5 Z. Wang, Y. Chong, J. D. Joannopoulos, and M. Soljačić, Nature **461**, 772 (2009).
6 S. A. Skirlo, L. Lu, and M. Soljačić, Phys. Rev. Lett. **113**, 113904 (2014).
7 F. D. M. Haldane, Phys. Rev. Lett. **61**, 2015 (1988).
8 F. D. M. Haldane, and S. Raghu, Phys. Rev. Lett. **100**, 013904 (2008), arXiv: cond-mat/0503588.
9 M. Hafezi, S. Mittal, J. Fan, A. Migdall, and J. M. Taylor, Nat. Photon. **7**, 1001 (2013), arXiv: 1302.2153.
10 Z. Yang, F. Gao, X. Shi, X. Lin, Z. Gao, Y. Chong, and B. Zhang, Phys. Rev. Lett. **114**, 114301 (2015), arXiv: 1411.7100.
11 Z. Yang, and B. Zhang, Phys. Rev. Lett. **117**, 224301 (2016), arXiv: 1601.07966.
12 Y. G. Peng, C. Z. Qin, D. G. Zhao, Y. X. Shen, X. Y. Xu, M. Bao, H. Jia, and X. F. Zhu, Nat. Commun. **7**, 13368 (2016), arXiv: 1508.06243.
13 Y. Ding, Y. Peng, Y. Zhu, X. Fan, J. Yang, B. Liang, X. Zhu, X. Wan, and J. Cheng, Phys. Rev. Lett. **122**, 014302 (2019).
14 X. Zhang, Z. K. Lin, H. X. Wang, Z. Xiong, Y. Tian, M. H. Lu, Y. F. Chen, and J. H. Jiang, Nat. Commun. **11**, 65 (2020), arXiv: 1811.05514.
15 Z. Yang, F. Gao, and B. Zhang, Sci. Rep. **6**, 29202 (2016), arXiv: 1504.02655.
16 M. Yan, J. Lu, F. Li, W. Deng, X. Huang, J. Ma, and Z. Liu, Nat. Mater. **17**, 993 (2018).
17 S. Y. Yu, C. He, Z. Wang, F. K. Liu, X. C. Sun, Z. Li, H. Z. Lu, M. H. Lu, X. P. Liu, and Y. F. Chen, Nat. Commun. **9**, 3072 (2018).
18 S. Li, D. Zhao, H. Niu, X. Zhu, and J. Zang, Nat. Commun. **9**, 1370 (2018).
19 P. Wang, L. Lu, and K. Bertoldi, Phys. Rev. Lett. **115**, 104302 (2015), arXiv: 1504.01374.
20 S. H. Mousavi, A. B. Khanikaev, and Z. Wang, Nat. Commun. **6**, 9682 (2015), arXiv: 1507.03002.
21 C. Brendel, V. Peano, O. Painter, and F. Marquardt, Phys. Rev. B **97**, 020102 (2018).
22 W. Song, W. Sun, C. Chen, Q. Song, S. Xiao, S. Zhu, and T. Li, Laser Photon. Rev. **14**, 1900193 (2020).
23 W. Wang, Y. Jin, W. Wang, B. Bonello, B. Djafari-Rouhani, and R. Fleury, Phys. Rev. B **101**, 024101 (2020).
24 Z. Q. Yang, Z. K. Shao, H. Z. Chen, X. R. Mao, and R. M. Ma, Phys. Rev. Lett. **125**, 013903 (2020).
25 X. Wu, Y. Meng, J. Tian, Y. Huang, H. Xiang, D. Han, and W. Wen, Nat. Commun. **8**, 1304 (2017), arXiv: 1703.04570.
26 X. S. Wang, H. W. Zhang, and X. R. Wang, Phys. Rev. Appl. **9**, 024029 (2018).
27 K. Ding, G. Ma, M. Xiao, Z. Q. Zhang, and C. T. Chan, Phys. Rev. X **6**, 021007 (2016), arXiv: 1509.06886.
28 K. G. Makris, R. El-Ganainy, D. N. Christodoulides, and Z. H. Musslimani, Phys. Rev. Lett. **100**, 103904 (2008).
29 R. El-Ganainy, K. G. Makris, M. Khajavikhan, Z. H. Musslimani, S. Rotter, and D. N. Christodoulides, Nat. Phys. **14**, 11 (2018).
30 H. Zhao, X. Qiao, T. Wu, B. Midya, S. Longhi, and L. Feng, Science **365**, 1163 (2019).
31 X. Zhu, H. Ramezani, C. Shi, J. Zhu, and X. Zhang, Phys. Rev. X **4**, 031042 (2014).
32 R. Fleury, D. Sounas, and A. Alù, Nat. Commun. **6**, 5905 (2015).
33 D. Zhou, and J. Zhang, Phys. Rev. Res. **2**, 023173 (2020), arXiv: 1912.09631.
34 M. A. Miri, and A. Alù, Science **363**, eaar7709 (2019).
35 Z. Lin, H. Ramezani, T. Eichelkraut, T. Kottos, H. Cao, and D. N. Christodoulides, Phys. Rev. Lett. **106**, 213901 (2011), arXiv: 1108.2493.
36 H. Xu, D. Mason, L. Jiang, and J. G. E. Harris, Nature **537**, 80 (2016), arXiv: 1602.06881.
37 L. Feng, Z. J. Wong, R. M. Ma, Y. Wang, and X. Zhang, Science **346**, 972 (2014).
38 B. Peng, S. K. Özdemir, S. Rotter, H. Yilmaz, M. Liertzer, F. Monifi, C. M. Bender, F. Nori, and L. Yang, Science **346**, 328 (2014), arXiv: 1410.7474.
39 Y. Y. Chen, G. L. Huang, and C. T. Sun, J. Vib. Acoust. **136**, 061008 (2014).
40 X. Li, Y. Chen, R. Zhu, and G. Huang, Mech. Syst. Signal Proc. **149**, 107324 (2021).
41 Y. Liu, Z. Liang, J. Zhu, L. Xia, O. Mondain-Monval, T. Brunet, A. Alù, and J. Li, Phys. Rev. X **9**, 011040 (2019), arXiv: 1807.02285.
42 S. Weimann, M. Kremer, Y. Plotnik, Y. Lumer, S. Nolte, K. G. Makris, M. Segev, M. C. Rechtsman, and A. Szameit, Nat. Mater. **16**, 433 (2017).
43 M. Rosendo López, Z. Zhang, D. Torrent, and J. Christensen, Commun. Phys. **2**, 132 (2019).
44 H. Gao, H. Xue, Z. Gu, T. Liu, J. Zhu, and B. Zhang, Nat. Commun. **12**, 1888 (2021), arXiv: 2007.01041.
45 A. Ghatak, M. Brandenbourger, J. van Wezel, and C. Coulais, Proc. Natl. Acad. Sci. USA **117**, 29561 (2020), arXiv: 1907.11619.
46 M. I. N. Rosa, and M. Ruzzene, New J. Phys. **22**, 053004 (2020), arXiv: 2001.01817.
47 H. Zhou, C. Peng, Y. Yoon, C. W. Hsu, K. A. Nelson, L. Fu, J. D. Joannopoulos, M. Soljačić, and B. Zhen, Science **359**, 1009 (2018), arXiv: 1709.03044.
48 Z. Gong, Y. Ashida, K. Kawabata, K. Takasan, S. Higashikawa, and M. Ueda, Phys. Rev. X **8**, 031079 (2018), arXiv: 1802.07964.
49 N. Okuma, K. Kawabata, K. Shiozaki, and M. Sato, Phys. Rev. Lett. **124**, 086801 (2020), arXiv: 1910.02878.
50 W. Zhu, X. Fang, D. Li, Y. Sun, Y. Li, Y. Jing, and H. Chen, Phys. Rev. Lett. **121**, 124501 (2018), arXiv: 1803.04110.
51 W. Tang, X. Jiang, K. Ding, Y. X. Xiao, Z. Q. Zhang, C. T. Chan, and G. Ma, Science **370**, 1077 (2020).
52 X. Wu, Y. Meng, Y. Hao, R. Y. Zhang, J. Li, and X. Zhang, Phys. Rev. Lett. **126**, 226802 (2021).
53 L. H. Wu, and X. Hu, Phys. Rev. Lett. **114**, 223901 (2015).
54 Y. Yang, Y. F. Xu, T. Xu, H. X. Wang, J. H. Jiang, X. Hu, and Z. H. Hang, Phys. Rev. Lett. **120**, 217401 (2018).
55 B. Zhou, H. Z. Lu, R. L. Chu, S. Q. Shen, and Q. Niu, Phys. Rev. Lett. **101**, 246807 (2008), arXiv: 0806.4810.

Appendix Derivation of scattering matrix

The derivation of scattering matrix starts from the Hamiltonian in eq. (1) on the basis of $\{L_+, L_-, R_+, R_-\}$. The effective governing equation of the coupler can be written as:

$$\widehat{H}\psi = f\psi, \tag{a1}$$

where $\psi = (C_1, C_2, C_3, C_4)^{\mathrm{T}}$, C_1, C_2, C_3, and C_4 are the coefficients of the elements in $\{L_+, L_-, R_+, R_-\}$ respectively, f is the frequency. The Hamiltonian can be divided into two parts by separating k_y, which governs the propagation of the waves:

$$\widehat{H} = \widehat{H}_0 - k_y v_{\mathrm{F}} \widehat{\Pi}, \tag{a2}$$

where

$$\widehat{H}_0 = \begin{pmatrix} \frac{\omega_{\mathrm{F}}}{2\pi} & 0 & \eta & \zeta \\ 0 & \frac{\omega_{\mathrm{F}}}{2\pi} & \zeta & \eta \\ \eta & \zeta & \frac{\omega_{\mathrm{F}}}{2\pi} & 0 \\ \zeta & \eta & 0 & \frac{\omega_{\mathrm{F}}}{2\pi} \end{pmatrix}, \tag{a3}$$

and

$$\widehat{\Pi} = \begin{pmatrix} -1 & 0 & 0 & 0 \\ 0 & 1 & 0 & 0 \\ 0 & 0 & 1 & 0 \\ 0 & 0 & 0 & -1 \end{pmatrix}. \tag{a4}$$

The governing equation then can be rewritten as: $(\widehat{H}_0 - k_y v_{\mathrm{F}} \widehat{\Pi})\psi = f\psi$, and we move k_y to the right hand side: $v_{\mathrm{F}}^{-1}\widehat{\Pi}^{-1}(\widehat{H}_0 - f\ I_4)\psi = k_y\psi$. Here, the bands of interface states are linear near the Γ point, k_y can be well approximated to the first order, and we then have the substitution $k_y = -\mathrm{i}\partial/\partial y = -\mathrm{i}\partial_y$. So the governing equation about k_y can be changed into that about y: $v_{\mathrm{F}}^{-1}\widehat{\Pi}^{-1}(\widehat{H}_0 - f\ I_4)\psi = -\mathrm{i}\partial_y\psi$. For a system with finite height in y, the solution of ψ as a function of y can be given as: $\psi(y) = \varphi \mathrm{e}^{\mathrm{i}v_{\mathrm{F}}^{-1}\widehat{\Pi}^{-1}(\widehat{H}_0 - f\ I_4)y}$, where φ is independent of y. The transfer matrix for $\psi(y)$ on the basis of $\{L_+, L_-, R_+, R_-\}$ can be written as: $T = \mathrm{e}^{\mathrm{i}v_{\mathrm{F}}^{-1}\widehat{\Pi}^{-1}(H_0 - f\ I_4)y}$.

As the schematic illustration shown in Figure a1, wave coefficients located at $y=a$ are denoted as $\psi(a) = (L_{+,a}, L_{-,a}, R_{+,a}, R_{-,a})^{\mathrm{T}}$, and located at $y=b$ are denoted as $\psi(b) = (L_{+,b}, L_{-,b}, R_{+,b}, R_{-,b})^{\mathrm{T}}$, where "$L$" ("$R$"), subscripts "+" ("−"), and "a" ("b") indicate the coefficients of the interface states at the left (right) domain wall with up (down) pseudospin, and located at $y=a$ ($y=b$). The coefficients $\psi(b)$ can be solved from $\psi(a)$ with the transfer matrix T by

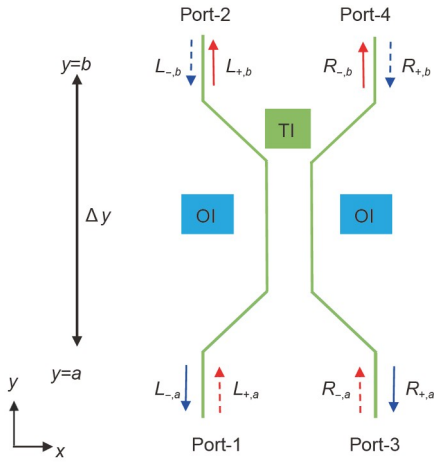

Figure a1 (Color online) Schematic of the topological coupler. The green lines indicate the domain walls of the topological coupler. The pseudospin up and pseudospin down topological interface states are indicated by arrows at each port and labeled by subscripts of "+" and "−", the direction of each arrow indicates the propagation direction of each state. States with positive group velocity are indicated by red arrows and those with negative group velocity are indicated by blue arrows, all incident states are indicated by dashed arrows, and outgoing states are indicated by solid arrows.

$$\begin{pmatrix} L_{+,b} \\ L_{-,b} \\ R_{+,b} \\ R_{-,b} \end{pmatrix} = \begin{pmatrix} T_{11} & T_{12} & T_{13} & T_{14} \\ T_{21} & T_{22} & T_{23} & T_{24} \\ T_{31} & T_{32} & T_{33} & T_{34} \\ T_{41} & T_{42} & T_{43} & T_{44} \end{pmatrix} \begin{pmatrix} L_{+,a} \\ L_{-,a} \\ R_{+,a} \\ R_{-,a} \end{pmatrix}, \tag{a5}$$

where T_{ij} is the (i,j) element of the **T** matrix. For a topological coupler with a wedge-shaped TI region, its Hamiltonian $\widehat{H}$ in eq. (1) is modeled as a function varying in y, and the final transfer matrix can be obtained by multiplying transfer matrices of each layer with a height of Λ. On the other hand, the transfer matrix T can be converted into a scattering matrix S by changing the basis:

$$\begin{pmatrix} L_{-,a} \\ L_{+,b} \\ R_{+,a} \\ R_{-,b} \end{pmatrix} = \begin{pmatrix} S_{11} & S_{12} & S_{13} & S_{14} \\ S_{21} & S_{22} & S_{23} & S_{24} \\ S_{31} & S_{32} & S_{33} & S_{34} \\ S_{41} & S_{42} & S_{43} & S_{44} \end{pmatrix} \begin{pmatrix} L_{+,a} \\ L_{-,b} \\ R_{-,a} \\ R_{+,b} \end{pmatrix}, \tag{a6}$$

where S_{ij} is the (i, j) element of the **S** matrix. $(L_{+,a}, L_{-,b}, R_{-,a}, R_{+,b})^{\mathrm{T}}$ contains the coefficients of the incident waves denoted by ψ_{in}, and $(L_{-,a}, L_{+,b}, R_{+,a}, R_{-,b})^{\mathrm{T}}$ contains the coefficients of scattering waves denoted by ψ_{out}. With the scattering matrix S, the outgoing waves (indicated by solid arrows in Figure a1) at each port then can be directly calculated from the incident waves (indicated by dashed arrows Figure a1) via: $\psi_{\mathrm{out}} = S\psi_{\mathrm{in}}$. When placing a pseudospin up source near port-1 to excite the topological coupler, the coefficients of the incident waves can be expressed as $\psi_{\mathrm{in}} = (1, 0, 0, 0)^{\mathrm{T}}$, and the outgoing waves at the i^{th} port then can be directly calculated by S_{i1}.